Ocean Modelling 87 (2015) 67–80

Contents lists available at ScienceDirect

Ocean Modelling

journal homepage: www.elsevier.com/locate/ocemod

Interactions between wind-blown snow redistribution and melt ponds in a coupled ocean–sea ice model

Olivier Lecomte [a,*], Thierry Fichefet [a], Daniela Flocco [b], David Schroeder [b], Martin Vancoppenolle [c]

[a] Georges Lemaître Center for Earth and Climate Research, Earth and Life Insitute, Université Catholique de Louvain, Place Louis Pasteur 3 – Boîte L4.03.08, 1348 Louvain-la-Neuve, Belgium
[b] Department of Meteorology, University of Reading, Earley Gate, PO Box 243, Reading RG6 6BB, UK
[c] Laboratoire d'Océanographie et du Climat (LOCEAN-IPSL), Centre National de la Recherche Scientifique (CNRS), Sorbonne Universités (UPMC, Univ Paris 06), 4 Place Jussieu, F-75005 Paris, France

ARTICLE INFO

Article history:
Received 12 May 2014
Received in revised form 28 November 2014
Accepted 3 December 2014
Available online 24 December 2014

Keywords:
Snow
Sea ice
Melt ponds
Model

ABSTRACT

Introducing a parameterization of the interactions between wind-driven snow depth changes and melt pond evolution allows us to improve large scale models. In this paper we have implemented an explicit melt pond scheme and, for the first time, a wind dependant snow redistribution model and new snow thermophysics into a coupled ocean–sea ice model.

The comparison of long-term mean statistics of melt pond fractions against observations demonstrates realistic melt pond cover on average over Arctic sea ice, but a clear underestimation of the pond coverage on the multi-year ice (MYI) of the western Arctic Ocean. The latter shortcoming originates from the concealing effect of persistent snow on forming ponds, impeding their growth. Analyzing a second simulation with intensified snow drift enables the identification of two distinct modes of sensitivity in the melt pond formation process. First, the larger proportion of wind-transported snow that is lost in leads directly curtails the late spring snow volume on sea ice and facilitates the early development of melt ponds on MYI. In contrast, a combination of higher air temperatures and thinner snow prior to the onset of melting sometimes make the snow cover switch to a regime where it melts entirely and rapidly. In the latter situation, seemingly more frequent on first-year ice (FYI), a smaller snow volume directly relates to a reduced melt pond cover.

Notwithstanding, changes in snow and water accumulation on seasonal sea ice is naturally limited, which lessens the impacts of wind-blown snow redistribution on FYI, as compared to those on MYI. At the basin scale, the overall increased melt pond cover results in decreased ice volume via the ice-albedo feedback in summer, which is experienced almost exclusively by MYI.

1. Introduction

Soon after the initiation of the summer surface melt on Arctic sea ice, meltwater starts accumulating in pools called melt ponds that usually cover up to 50–60% of the sea ice area during summer. The processes driving the formation and evolution of those melt ponds are well documented (e.g., Fetterer and Untersteiner, 1998; Perovich et al., 2002; Polashenski et al., 2012). The most important consequence of the pond formation with respect to the sea ice energy and mass balance is the critical drop in surface albedo wherever ponds form, triggering further ice surface and basal melt through the ice-albedo feedback. The crucial role of melt ponds in controlling the evolution of the sea ice albedo thus make them a key component of the polar climate system.

Serious efforts have already been invested in the representation of melt ponds in large-scale sea ice models (e.g., Pedersen et al., 2009; Flocco et al., 2010, 2012; Holland et al., 2012; Hunke et al., 2013). Those studies gave evidence that models are sensitive to the representation of melt ponds and showed that actually accounting for their influence on the ice-albedo feedback leads to consequential sea ice volume reductions. Even so, those models are not comprehensive yet and still lack a few of the processes driving the formation and evolution of melt ponds. Among them are snow-related processes.

The sea ice snow cover is one of the main short- and long- term controlling factors for melt pond distributions, for several reasons. The first is that freshwater from snow melt on sea ice participates to feeding the ponds as they start forming. Secondly, pooling

* Corresponding author.
E-mail address: olivier.lecomte@uclouvain.be (O. Lecomte).

http://dx.doi.org/10.1016/j.ocemod.2014.12.003
1463-5003/

meltwater may remain hidden by a thick snow cover as long as it has not melted entirely, affecting both the timing and intensity of the local albedo feedback that is triggered when ponds become visible. Lastly, the refreezing of meltwater at the base of the snow pack has been shown to create superimposed ice atop sea ice. Those locations of surficial ice formation may then turn into topographic high spots under snow dunes, between which ponds form (Freitag and Eicken, 2003; Polashenski et al., 2012; Petrich et al., 2012). Snow also has a more indirect but important impact on melt pond formation through its influence on ice permeability and surface topography. Superimposed ice formation (e.g., Eicken et al., 2004) and interposed ice formation within brine channels (e.g., Polashenski et al., 2012) alter the permeability of ice and thus the way meltwater is drained through the ice. Besides, by exerting control over the ice growth due to its insulating power, snow constrains the ice thermodynamic growth and thickness distribution. Melt pond formation is also very sensitive to the geometry and scale of snow depth distributions, which are extremely heterogeneous (e.g., Sturm et al., 2002), mostly due to blowing snow effects and to a frequently uneven sea ice surface topography. Depending on the nature of an ice floe, whether it is multi-year or seasonal, level or deformed, the wind tends to draw manifold snow drift features at its surface, such as dunes, sastrugi or accumulation patterns under the lee of sea ice pressure ridges (Sturm and Massom, 2009). In light of those elements, the question of the indirect influence of blowing snow on melt pond formation through the reshaping of the snow cover becomes legitimate, and may lead to different answers for different ice types.

In the present paper, we therefore aim at (1) simulating a realistic melt pond cover on Arctic sea ice, (2) understanding the large-scale influence of snow depth changes due to wind-blown snow redistribution on melt pond formation and evolution and (3) assess the similarity or dissimilarity of those impacts on first-year ice (FYI) and multi-year ice (MYI). Both because melt ponds are relatively uncommon and because their extensive observation is non-existent in the Southern Ocean, our study focuses on the Arctic. So as to achieve this work, the explicit melt pond formalism of Flocco and Feltham (2007) was incorporated into the Louvain-la-Neuve Sea Ice Model (LIM), which is fully coupled with the ocean general circulation model (GCM) NEMO-OPA (Nucleus for European Modelling of the Ocean – Ocean PArallelisé). In particular, LIM includes a snow scheme of intermediate complexity (Lecomte et al., 2013) and a newly developed parameterization of blowing snow effects, a novelty for such kind of model. The following section introduces the model, before the forcing and observations used in this study are described in Sections 3 and 4. In Section 5 and 6, we proceed to the assessment and intercomparison of two forced-atmosphere configuration simulations. The first one is a control run evaluated against observations and the second is a simulation designed to appraise the effects of enhanced snow drift on snow depth, melt pond area and sea ice volume. The analyses are performed using long-term mean sea ice and snow diagnostics over the Arctic Basin. Section 7 finally summarizes the results.

2. Model description

2.1. Ocean and sea ice

NEMO-LIM (Nucleus for European Modeling of the Ocean – Louvain-la-Neuve Sea Ice Model) is a state-of-the-art global coupled ocean–sea ice model. Its ocean component is the GCM OPA (Ocean PArallelisé, version 9) and is fully documented in Madec (2008). The thermodynamic-dynamic sea ice model, on the other hand, is LIM3 (LIM, version 3) and is coupled to the ocean component following Goosse and Fichefet (1999). This model, comprehensively described in Vancoppenolle et al. (2009), includes an explicit representation of the subgrid-scale distributions of ice thickness, enthalpy, salinity and age. Sea ice thermodynamics are computed for each sea ice thickness category following Bitz and Lipscomb (1999) and halodynamics use empirical parameterizations for gravity drainage and percolation of brines. The elastic-viscous-plastic (EVP) rheology of Hunke and Dukowicz (1997) in the C-grid formulation of Bouillon et al., 2009 is used to solve the sea ice dynamics. We run the model in the same configuration as in Lecomte et al. (2013), i.e., on the global tripolar ORCA1 grid of the ocean model (1 degree resolution), with 5 ice thickness categories (each of them being divided into 5 layers for sea ice halo-thermodynamics) and 42 vertical levels in the ocean. Spurious model drift in salinity is prevented by a sea surface restoring term (Levitus, 1998, toward climatological values of) in the freshwater budget.

2.2. Snow and melt ponds

To account for the interactions between snow drift and melt pond formation, a parameterization of wind-blown snow redistribution and an explicit melt pond scheme were incorporated to NEMO-LIM. With regard to the melt pond component, new sea ice tracers (i.e., melt pond fraction, melt pond volume and ice lid volume atop melt ponds) are technically required to track the evolution of the total liquid water volume and melt pond properties in time and space. As all sea ice tracers, these variables are affected by sea thermodynamic and dynamic redistribution processes. However, melt ponds in the model remain "virtual" since their proper physical treatment as concrete liquid layers on sea ice is not taken into account. They are used for sea ice albedo computation only. Here, in order to include the impact of the presence of liquid water on snow thermodynamics, the snow scheme we use was modified. We thus first introduce the main characteristics of this snow thermodynamic scheme (Section 2.2.1) before presenting the changes made with respect to the latter processes (Section 2.2.2). In the following subsection, the melt pond model and the way melt pond-related variables are used to calculate the albedo are described, before finally documenting the blowing snow parameterization.

2.2.1. Initial thermodynamic snow model

The thermodynamic snow scheme we use was developed in previous studies (Lecomte et al., 2013, for its comprehensive description, see). It is multilayer, with time and space dependent snow thermo-physical properties (i.e., density and thermal conductivity) and includes heat conduction through the snow, penetration and absorption of solar radiation in the uppermost snow layers (Järvinen and Lepparanta, 2011, following Beer's law and extinction coefficient from), surface melt or sublimation based on the imbalance of the surface heat budget and a representation of snow ice formation based on Fichefet and Morales Maqueda, 1997.

2.2.2. Water infiltration into the snow

So as to account for wet snow properties and the refreezing of freshwater into the snow, the following model modifications were made, as compared to Lecomte et al. (2013). Because snow gets saturated with water very quickly (Jordan et al., 2008; Sturm and Massom, 2009), we assume that the snow cover is wet whenever the liquid water reservoir is not empty (for a given ice category, in a single grid cell). As in Hunke et al. (2013), water infiltration in the snow is computed based on the amount of water available and the volumes being possibly occupied in snow, depending on its density. The mass fraction of liquid water relative to the total mass of water and snow in a layer is then used to alter the snow thermal conductivity, calculated as a weighted mean of snow and freshwater thermal conductivities. Finally, freshwater that may

refreeze in case of divergence of the conductive heat fluxes going in and out of a saturated snow layer is given by:

$$-L_f \frac{dm_{rfw}}{dt} = fc_s^{in} - fc_s^{out}, \quad (1)$$

where L_f is the latent heat of fusion, m_{rfw} the mass of refrozen freshwater, and fc_s^{in} and fc_s^{out} the conductive heat fluxes at the interfaces of the snow layer, respectively. The adopted formalism is similar to Cheng et al., 2006, except that the refrozen water does not become part of the sea ice mass underneath. Instead, it is incorporated to the mass of snow, affecting its density and slackening the early stages of the snow melt. This process acts as a sink for the melt pond water, as long as snow remains present and water volumes are small. Note that, on the contrary, in case of convergent conductive heat fluxes in a snow layer at the melting point, snow melts internally and becomes a source for the freshwater reservoir.

2.2.3. Melt ponds and impact on sea ice albedo

The melt pond model. The melt pond formulation we use is the one of Flocco and Feltham (2007) and the way it was incorporated into our sea ice model is very similar to the works of Flocco et al. (2010, 2012). In the real world melt ponds form in natural depressions on the sea ice topography starting from snow melting. Small scale studies (see Scott and Feltham, 2010), impose a sea ice topography and include a snow cover to then redistribute the sea water depending on different sea ice elevation. They show that sea ice topography drives the formation and evolution of melt ponds on sea ice. This approach is not directly usable in a GCM where a real sea ice topography is not available. Flocco et al. (2010, 2012) introduce an idealized concept of water redistribution assuming that the small scale process of water filling up the thinnest ice first, can be upscaled and the total meltwater volume calculated in each time step can be placed on the thinner ice categories first. The ice in the whole grid cell is rigid and assumed to be in hydrostatic equilibrium. Changes in water volume retained on the ice are calculated in each time step depending on the manifold source and sink processes described hereafter. Following the approach of Flocco et al. (2010), the melt water is redistributed among ice thickness categories, depending on their surface height and the volume of their snow cover in order to determine the melt pond area fraction and depth.

In order to couple the sea ice and melt pond models, three new tracers were added: the melt pond volume, area and ice lid volume in case ponds refreeze (all three tracers are expressed per unit area of ice). For the sake of clarity, Fig. 1 summarizes the freshwater balance leading to the calculation of melt pond tracers during a model time step. Melt pond volume is initially fed by snow/sea ice surface melt, snow internal melt and rain. The meltwater volume in the model may then be reduced by physical infiltration and refreezing of water into the snow, as presented in Section 2.2.2. At each time step, a fraction of this volume (depending on the total ice concentration, Holland et al., 2012) is lost by lateral run-off through cracks or ice floe edges. If the pond surface is above the sea level, the vertical drainage of meltwater through permeable sea ice into the ocean is computed following Darcy's Law, as a function of the pressure head relative to the sea level and the ice permeability. Sea ice permeability is computed as proposed by Golden et al. (2007):

$$\Pi = 3(1-\phi^3) \times 10^{-8}, \quad (2)$$

where ϕ is the solid fraction within the ice, calculated as in Feltham et al. (2006):

$$\phi = \frac{c_{bulk} - C(T)}{C_i - C(T)}. \quad (3)$$

c_{bulk} is the bulk salinity of the ice, C(T) is salt concentration in brines and C_i the salt concentration in the ice crystals (set to zero here). The least permeable layer within the ice determines the vertical drainage rate. When the surface heat budget gets negative, melt ponds start refreezing and the growth rate of the ice lid forming on top of the melt pond is calculated using Stefan's law. The ice lid may undergo further growth or melt depending on the surface heat balance. The pond volume is also affected by sea ice advection and deformation. Fractions for melt pond and ice lid volume lost during sea ice ridging or rafting were added to the model. A few test cases showed that changing those parameters induced almost no change in pond coverage in the model. At this stage, it is not clear whether this weak sensitivity was to be expected. We therefore prescribed the value of those fractions to 50%, as it was already the case for snow in LIM3. As in Flocco et al. (2012), the fraction of ice covered by ponds in each category is limited by a prescribed value that is function of its thickness: $a_{pmax} = 0.832\% - h_i * 0.024$. Once the melt pond area fraction, depth and ice lid thickness are calculated, they are used to retrieve the effective albedo of the pond covered ice.

Albedo calculation. In order to account for melt pond tracers in the albedo calculations, the melt pond albedo is first computed as a function of its depth, as in Lecomte et al. (2011):

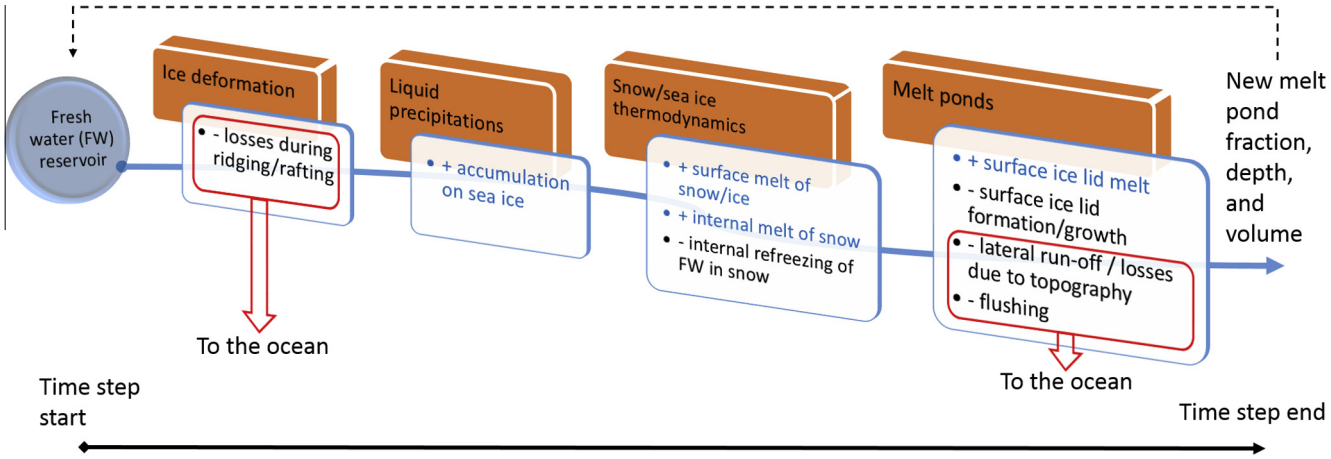

Fig. 1. Evolution of the freshwater reservoir in a grid cell during a model time step. At the time step start, this reservoir is equal to the melt pond volume. All source and sink processes listed in this diagram are described in Section 2.2.3.

$$\alpha_p = \begin{cases} \alpha_w - (\alpha_w - \alpha_i)e^{\frac{-h_p}{\omega}} & \text{if no active ice lid and active melt pond,} \\ \alpha_{bi} & \text{if active ice lid,} \end{cases} \quad (4)$$

where α_i and $\alpha_w = 0.30$ are the snow-covered ice and deep pond albedo, h_p is the pond depth in m and ω is a constant scale factor in the same units as h_p. α_i is computed as a function of the surface wetness (melting conditions), cloud cover, snow depth and ice thickness (Shine and Henderson-Sellers, 1985), as in the former version of the model without melt ponds. α_{bi} is the albedo of bare ice, equal to 0.58. Note that, like in Flocco et al. (2012), melt ponds/ice lids are optically active and affect the sea ice albedo only when they are deeper/thicker than a critical value of 1 cm. Then, the mean albedo of the various surface types weighed by their relative coverage of the ice cover is calculated:

$$\alpha = \alpha_i(1 - a_p) + \alpha_p a_p, \quad (5)$$

where a_p is the melt pond fraction of ice area.

2.2.4. Blowing snow

Blowing snow (or snow drift) on sea ice tends to redistribute the snow mass from thin level ice to thicker and deformed ice. The process smoothes out small and high frequency changes in sea ice topography while enhancing larger topographic features such as pressure ridges (Sturm et al., 2002). Usually, the "blowing snow" term includes several sub-processes such as snow erosion and motion by saltation or suspension (snow transport by winds). Snow drift is also a sublimation-enhancing process, facilitating the sublimation of grains thrown in suspension (Déry and Yau, 2002). The impacts of such mechanisms are well documented (e.g., Déry and Tremblay, 2004; King et al., 2008; Sturm and Massom, 2009; Leonard and Maksym, 2011). Most importantly, snow that is ripped off the pack and transported by winds may be lost into leads, or redeposited on the ice, altering the spatial distribution of snow depths. As the wind direction shifts or the floe rotates, snow undergoes further erosion that may affect the surface drag coefficient and the dynamic response of sea ice to the wind forcing. Given the difficulty of establishing a new parameterization due to the lack of observations available for this specific process, we only thought to represent the zero order impact of blowing snow on the subgrid-scale snow depth distribution. To our knowledge, it is the first time such developments are made in a large-scale coupled ocean–sea ice model.

The usual conservation equation for a global state variable such as the total snow mass per unit area m_s on a single ice thickness category is:

$$\frac{\partial m_s}{\partial t} = -\nabla(m_s\mathbf{u}) + \Psi^{m_s} + \Theta^{m_s} + \Phi, \quad (6)$$

where $-\nabla(m_s\mathbf{u})$ represents the horizontal advection of snow due to sea ice motion, Ψ^{m_s} the effects of the mechanical redistribution of sea ice on snow, Θ^{m_s} the changes in snow mass due to the thermodynamic processes described in the previous two sections and Φ the wind-redistribution of snow. The later term may be written as:

$$\Phi = \Phi_{local} + \Phi_{nonlocal}, \quad (7)$$

the local term accounting for redistribution of the snow mass over the sea ice thickness categories, and the non local one representing the snow transport from grid cell to grid cell. For the sake of simplification, we assume that, at the synoptic scale of a storm, the snow mass being transported out of a grid cell matches the amount of snow that is transported in and we therefore neglect the non local effect of blowing snow. The validity of this assumption may depend on the horizontal resolution of the model grid, but would require the coupling with an atmospheric circulation model in order to be properly tested. Φ_{local} may be separated into two terms:

$$\Phi_{local} = \Phi^T_{local} + \Phi^R_{local}, \quad (8)$$

where Φ^T_{local} and Φ^R_{local} are the ripping out and re-deposition rates, respectively. Based on the thought, that snow drift mainly depends on wind speed, snow surface properties and sea ice surface topography (e.g., Sturm and Massom, 2009), we formulate those rates in a simple way, as illustrated by Fig. 2. We assume that the mass flux of snow removed from the pack and transported by winds is (1) negatively proportional to the snow density (packed snow is less erodable than light snow), (2) proportional to the wind speed, as long as it is greater than a threshold velocity $V^\star$ and (3) inversely proportional to the standard deviation of the ice thickness distribution σ_{ITD} (i.e., over the thickness categories) in a grid cell. In reality, snow drift quantity is proportional to the cube of the friction velocity (e.g., Schmidt, 1982) but here, given that blowing snow is a small scale process that cannot be represented in such a GCM as it occurs in the real world, we only kept the basic relationship tying stronger winds to greater erosion. $V^\star$ is computed as:

$$V^\star = \frac{\rho_s - \beta}{\alpha}, \quad (9)$$

where ρ_s is the snow density and α and β are coefficients that were retrieved from a linear regression of observations relating the seasonal mean wind speed to the actual snow density ($\alpha = 44.6$ kg m^{-4} s and $\beta = 174$ kg m^{-3}, Lecomte et al., 2013). Physically, $V^\star$ represents the seasonal mean wind velocity that is required to make the snow pack as dense as ρ_s, and it is assumed that blowing snow will start only as soon as the instantaneous wind speed exceeds this value. σ_{ITD} on the other hand is considered as a roughness length limiting the snow drift in case of large disparities in ice thicknesses (represented by a large σ_{ITD}). Given the relatively poor ice deformation diagnostics in current sea ice models, we chose this simple solution instead. However, no observation clearly supports this approximation, so using the ice thickness distribution to derive surface roughness is only a temporary solution. The issue will need to be better addressed as soon as reliable sea ice topography tracers are available in such models. Some promising rheology formalisms, adequate to this purpose, may become operational in sea ice models in a near term future (e.g., Girard et al., 2011). A constant mass flux coefficient γ is used to tune the relationship between Φ^T_{local} and the wind speed. For a same wind velocity, a higher γ induces a larger snow mass removed from the ice (and potential losses into leads), and conversely. Since the fine calibration of this parameter based on extensive observations is currently impossible, it was adjusted (to the standard value of 10^{-5} kg m^{-2}) to produce mass fluxes that are physically plausible ($\sim$1–10 g m^{-2} s^{-1}, compared to Sugiura et al. (1998)) and provide an Arctic mean snow volume comparable to the one of Lecomte et al. (2013) (reference run). The rationale is that the former model version of Lecomte et al. (2013) included an even simpler parameterization of direct snowfall losses into the ocean based on the total ice concentration in grid cells only. This formulation was disabled and replaced by the present snow redistribution scheme but preserving the mean Arctic snow volume, which seemed realistic. In our results below, we assess the sensitivity of our model to this new parameterization and its influence on melt pond distributions.

A fraction of the total mass of snow transported by winds, proportional to the area of open water in the grid cell, is then lost in leads and the rest is redistributed among ice thickness categories via Φ^R_{local}, proportionally to their relative coverage of the total ice area. Again, this was done on the simple assumption that wind-blown snow redistribution on sea ice is largely dependent on the size of open water areas between ice floes (Leonard and Maksym, 2011). However, the actual geometrical distribution of cracks in the ice is likely as much important as the total area of open water for snow losses into the ocean. Parameterizing the shape and size

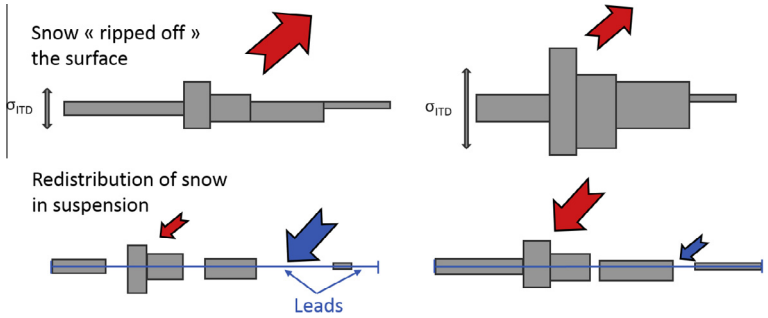

Fig. 2. Schematic representation of the snow redistribution by winds on the subgrid-scale distribution of ice thicknesses in the model. Gray boxes represent the ice thickness categories. The height and width of each box symbolizes the thickness and area coverage of each category. σ_{ITD} stands for the standard deviation of the ice thicknesses (from categories) within a grid cell. For instance, using five ice categories in the model provides five ice thickness values per grid cell. σ_{ITD} is the standard deviation over those five values. Top plots show how σ_{ITD} influences the snow mass fluxes (upward red arrows) from the ice during blowing snow transport. Basically, flat ice (translating in small σ_{ITD}) enables stronger erosion rates, hence larger mass fluxes of snow removed from the ice when snow drift is triggered, and conversely for deformed ice. Bottom plots show how the wind-transported snow mass is partitioned between mass fluxes to the ice (downward red arrows) and a mass flux to the ocean through the cracks between the ice floes (blue arrows) during redeposition (see Section 2.2.4). The fraction of the total transported snow mass that is lost in leads is proportional to the area of open water in the grid cell. (For interpretation of the references to colour in this figure caption, the reader is referred to the web version of this article.)

of leads or increasing the resolution to explicitly resolve them would likely influence the redistribution scheme behavior. Adressing this problem is a long term perspective for the improvement of the sea ice model and snow redistribution scheme used here.

3. Forcing and setup

Except for precipitation, the model is driven by the same forcing fields as in Lecomte et al. (2013), all spatially interpolated onto the ORCA1 grid. NCEP/ NCAR daily reanalyses of 2 m air temperature and 10 m $u-$ and $v-$ wind components of Kalnay et al. (1996) are used, together with monthly climatologies of total cloudiness and relative humidity of Berliand and Strokina (1980) and Trenberth and Large (1989), respectively. River runoff rates are taken from Dai and Trenberth (2002). Usually, we use the climatology of Large and Yeager (2004) as precipitation input to our model. Here, in order to get a more realistic regional variability of the snowfall, we added the precipitation anomalies from DFS5.2 (DRAKKAR Forcing Set, version 5, Dussin and Barnier, 2013) to the climatology. The making of DFS5 follows the same method as in Brodeau et al. (2010), applied on the ERA-interim reanalysis product (Simmons et al., 2007; Dee et al., 2011). The reason why the full DRAKKAR precipitation forcing set was not used was to avoid introducing a large bias in model results due to a bias in the mean precipitation rates (as compared to the former climatology), which would have required further tuning of the model. Surface heat fluxes (radiative and turbulent) are derived from Goosse (1997), and the wind stress over sea ice is calculated with a quadratic bulk formula and a drag coefficient $C_a = 1.40 \times 10^{-3}$.

Since the DFS5 precipitation data we use are available from 1979, model simulations are performed from 1979 to 2011. In Sections 5 and 6, the first three years of the simulations are not considered in order to let a short model spin-up before we start the analysis. The initial state for all sea ice covered regions of the Arctic Basin (defined by the locations where the sea surface temperature is below 0 °C) is set to 3.5 m (0.3 m) for ice (snow) thickness, 0.95 for ice concentration, 270 K for snow and ice temperatures and 6 PSU for sea ice salinity. The snow scheme is used with 3 layers advected horizontally, but the vertical resolution is refined to 6 layers in the thermodynamics. Ocean temperatures and salinities are initialized from Levitus, 1998 climatological values. The ocean model runs hourly and calls to the sea ice model are made every 6 time steps.

4. Observations

In the result sections below, we compare our simulations to several observational datasets. We use Advanced Microwave Scanning Radiometer (AMSR-E), Special Scanning Microwave Imager (SSM/I) and Scanning Multichannel Microwave Radiometer (SMMR) sea ice extent data, processed by the NASA Team and Bootstrap algorithms and distributed by the NSIDC (National Snow and Ice Data Center) (Comiso and Nishio, 2008). In addition, large-scale airborne surveys of snow depth and ice thickness from Operation IceBridge (Kurtz et al., 2012) are used to evaluate our modeled snow depth and ice thickness distributions on Arctic MYI (defined as the ice remaining at the time of the minimum extent). In order to properly compare the model outputs with those observations, the data were interpolated on the ORCA1 grid and used to generate a mask for model fields. Therefore, whenever the model results are compared to IceBridge observations in the following, it is done only where observations at matching locations are available. MODIS (Moderate Resolution Imaging Spectroradiometer) melt pond fraction satellite data over 2000–2011 (MODIS, 2013; Rösel et al., 2012) were also used for comparison with simulated melt pond spatial distributions. The dataset, initially on the 12.5 km × 12.5 km polar stereographic grid of the NSIDC, was interpolated on the ORCA1 grid for comparison with model outputs.

5. Control run (CTL) versus observations

5.1. Results

Here, we first analyze a control run (hereafter referred to as CTL) performed through 1982–2011, using the model as described in the previous sections. We compare CTL against the set of observations mentioned above to appraise the model skills in simulating the sea ice extent, volume, snow and melt pond cover.

5.1.1. Sea Ice

Fig. 3 shows the simulated and observed mean seasonal cycle of sea ice extent through 1982–2011, and the simulated mean cycle of sea ice volume over the same period for CTL. Sea ice extents produced by the model is in good agreement with the observed ones, except for the summer minimum, which is underestimated by half a million square kilometers and shifted from September to August. Although sea ice extent seems to be well reproduced in the

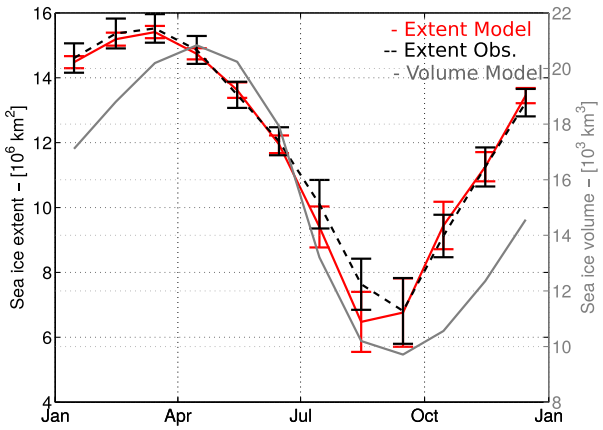

Fig. 3. Simulated (red) and observed (Comiso and Nishio, 2008, NASA data, dashed black) mean annual cycles of Arctic sea ice extent over 1982–2011 and simulated mean annual cycle of Arctic sea ice volume (gray) over the same period. Error bars represent the standard deviation of the monthly extents, over the simulation period. (For interpretation of the references to colour in this figure caption, the reader is referred to the web version of this article.)

simulation, sea ice volume appears too low, with a maximum and a minimum of 20.8 $\times$ 10^3 km^3 and 9.7 $\times$ 10^3 km^3, respectively. Comparing, for instance, these values with PIOMAS estimates (Zhang and Rothrock, 2003) would lead to a mean underestimation of the sea ice volume of about 20%. In comparison to the reference simulation of Lecomte et al. (2013), without the new processes (i.e., melt pond representation and blowing snow), the Arctic mean sea ice extent is similar, but the volume is reduced by about 40% in winter and 50% in summer (reasons are discussed in section 5.2).

The simulated ice thickness distributions (ITDs) (Fig. 4) consistently show an underestimation of IceBridge ice thicknesses (Kurtz et al., 2012), mainly including MYI data. In March, the coverage of ice in the first three categories of ice thickness in the model is overestimated by up to 15% (for category 2 and 3), while the amount of ice in the last two categories is largely underestimated. In particular, all the ice thicker than 4 m observed during IceBridge flights is missing in the simulation. In April, the IceBridge ITD indicates that ice thinner than 2 m has kept forming since March and the relative coverage of 0–2.3 m thick ice has increased to the cost of 2.3–5.5 m thick ice. Consequently, the biases between CTL and IceBridge ITDs are reduced, but the simulated sea ice thicknesses remain thinner than the observed ones in general, with an underestimation of 2.3–3.8 m thick ice of ~13% and 4–5.5 m thick ice that is still completely missing.

5.1.2. Snow

Like in Lecomte et al. (2013), snow depths are relatively well simulated by the model overall, as suggested by Fig. 5 which shows the snow depth distributions (SDD) in CTL versus IceBridge data. As for ice thickness, the simulation exhibits a bias towards thinner snow, with a large proportion of 0–5 cm deep snow (12% in March, 9% in April, against 3% and 5% for IceBridge, respectively) and an underestimation of 30–45 cm deep snow by ~3%. Note that the simulation features a second mode in snow depth around 45–60 cm deep snow, which is not visible in the observations.

5.1.3. Melt ponds

Fig. 6 depicts the mean summer cycles of the main melt pond diagnostics in the model, namely the area fraction of ice covered in ponds, melt pond depth, ice lid thickness (refreezing atop the pond) and the surface broadband albedo of pond covered ice. Melt ponds start forming in May, and reach their maximum coverage of 0.15 for exposed-ponds (i.e., still uncovered by a refreezing ice lid) and 0.28 for all-ponds in mid-July. The maximum depth of melt ponds (~0.25 m) is reached a month later, in August, before ponds shrink rapidly in September due to surface refreezing. The albedo consistently follows the evolution of the sea ice surface state, dropping from ~0.8 to ~0.3 in mid-August as melt ponds develop and rising again as soon as their refreezing stage begins. Specifically looking at the agreement between simulated exposed-ponds and MODIS observations of melt ponds (MODIS, 2013; Rösel et al., 2012) yields a good timing of the melt pond development in the model, and a consistent maximum value for the mean melt pond fraction over the Arctic Basin (Fig. 7), although it is underestimated in early season. As stated in Rösel et al. (2012), MODIS melt pond fractions are overestimated in late summer season since their algorithm misclassifies areas of thin ice as ponded ice. Therefore, our simulated melt pond fractions may be realistic during this period. The generally low pond fraction in the Central Arctic Ocean is emphasized by Figs. 8 and 9, which display the mean geographical distributions of melt pond fraction, depth and difference between CTL and MODIS satellite melt pond fractions through June-September for 2000–2011 (period with available observations). The MODIS maximum melt pond concentrations are below those observed on the field (Polashenski et al., 2012) and are especially

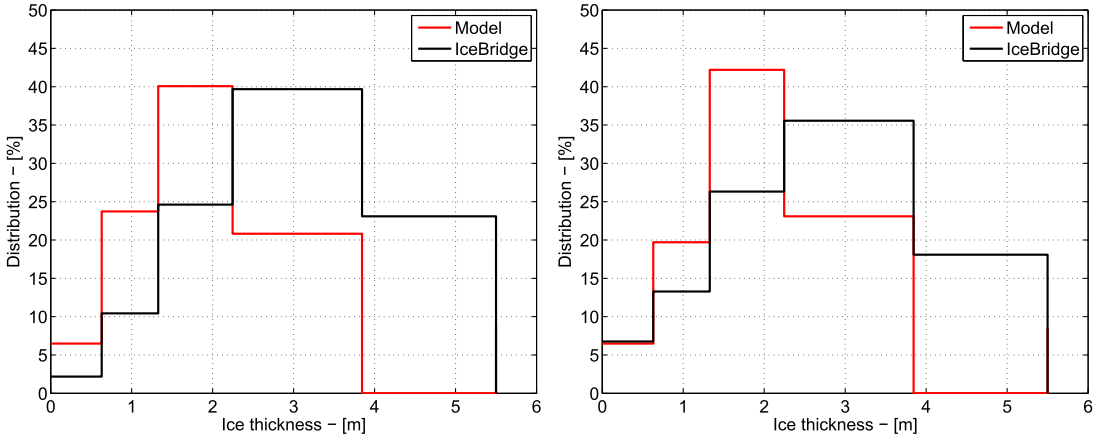

Fig. 4. Ice thickness distributions (ITDs) as simulated by the model (red) and observed during IceBridge flights (Kurtz et al., 2012) (black), in March (left panel) and April (right panel). Simulated ITDs are averaged over the analysis period (1982–2011). Bounds in sea ice thickness correspond to those from the ice thickness distribution in the model. (For interpretation of the references to colour in this figure caption, the reader is referred to the web version of this article.)

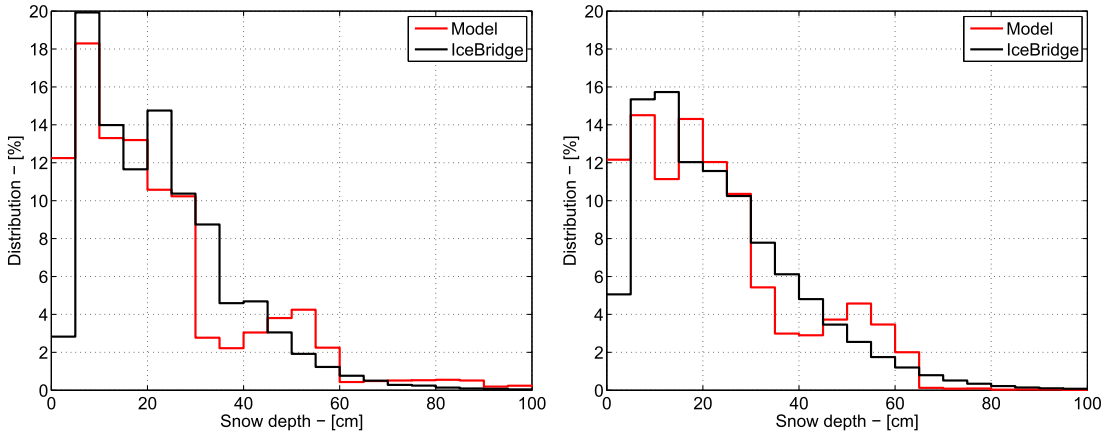

Fig. 5. Snow depth distributions (SDDs) as simulated by the model (red) and observed during IceBridge flights (Kurtz et al., 2012) (black), in March (left panel) and April (right panel). Simulated SDDs are averaged over the analysis period (1982–2011). (For interpretation of the references to colour in this figure caption, the reader is referred to the web version of this article.)

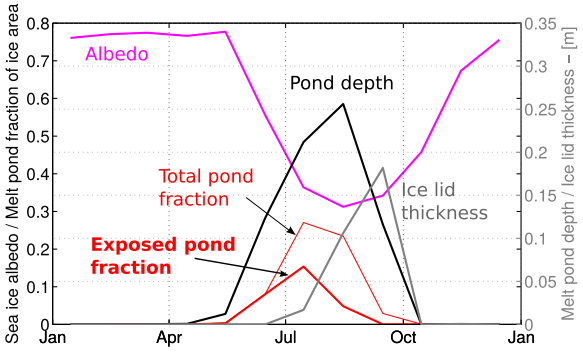

Fig. 6. Mean annual cycles of melt pond-related diagnostics (through 1982–2011). The purple curve represent the ponded-ice clear sky broadband albedo. The bold and light red curves depict the exposed (not covered by an ice lid) and total melt pond fraction of ice area, respectively. Black and gray curves read on the right hand y-axis, and picture the pond depth and ice lid thickness, respectively. (For interpretation of the references to colour in this figure caption, the reader is referred to the web version of this article.)

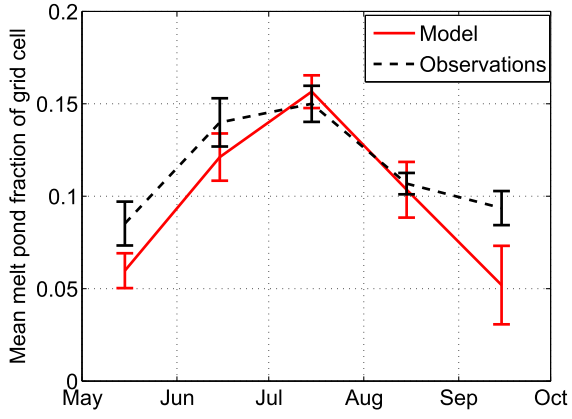

Fig. 7. Mean seasonal cycles of melt pond fraction (over 2000–2011), expressed as a fraction of grid cell, from the model (red) and from MODIS observations (Rösel et al., 2012, dashed black). Error bars represent the standard deviation of the monthly melt pond fractions over 2000–2011. (For interpretation of the references to colour in this figure caption, the reader is referred to the web version of this article.)

not in agreement with observations in early and late season (e.g., see corresponding discussion section). This product is therefore far from absolute but provides a baseline for the model evaluation at the basin scale. The maximum melt pond fractions (~0.4) are found in July in the Canadian Archipelago and in the transitional region between the Laptev Sea and the Arctic Ocean, whereas very deep melt ponds (0.5 m) are found in the Canadian Archipelago only. Overall, melt ponds tend to remain shallow in the marginal sea ice zone of the eastern basin (with fractional coverages of up to 0.35), while they get deeper (up to ~0.35 m) on the MYI of the western and central basin. These opposite patterns are particularly noticeable in July, and to a lesser extent in August. Fig. 9 shows a general model tendency to underestimate the melt pond relative coverage, especially in the central basin, while some coastal regions are significantly over-covered (overestimation by 0.15–0.25 in July).

5.2. Discussion

The sea ice volume loss observed in CTL compared to a no-melt pond run such as in Lecomte et al. (2013) is huge (up to 50% volume loss in summer, not shown) but consistent with Flocco et al., 2012 (using the same melt pond scheme in a similar multi-category sea ice model), in which they noticed a ~40% volume loss between pond and no-pond configurations. The early occurrence of the minimum ice extent on the other hand is not realistic with regard to present-day observations, but typical of a low ice volume simulation (Lecomte et al., 2013), where the ice has a weaker thermodynamical inertia and melts faster in summer. Besides, in the simulation, the minimum ice extent consistently occurs at the time of the maximum unfrozen melt pond volume.

The slight underestimation of snow depths compared to IceBridge observations is primarily explained by the underestimation of the ice thickness itself, suggesting younger ice overall that is not formed yet in the early accumulation season and therefore misses some snowfall events (Sturm and Massom, 2009). However, this is to balance with the fact that IceBridge sensors may also have trouble discriminating the thinnest snow (Webster et al., 2014) classes. The shape of the SDDs, in Fig. 12 especially, depict two maxima at 20–30 cm and 50–60 cm, while snow of moderate depth (~30 cm) seems to be lacking. Such bimodal SDDs are due to the ice type mixing in grid cells. First-year ice, represented by the thinnest ice thickness categories, is covered by relatively thin snow while older FYI or MYI (represented by intermediate and thick ice classes, respectively) carry thicker snow covers. Depending on the relative area coverage of each ice thickness category in grid cells, peaks associated to snow on each ice type appear more or less distinctly in the SDDs. This was observed in some individual data sets of the

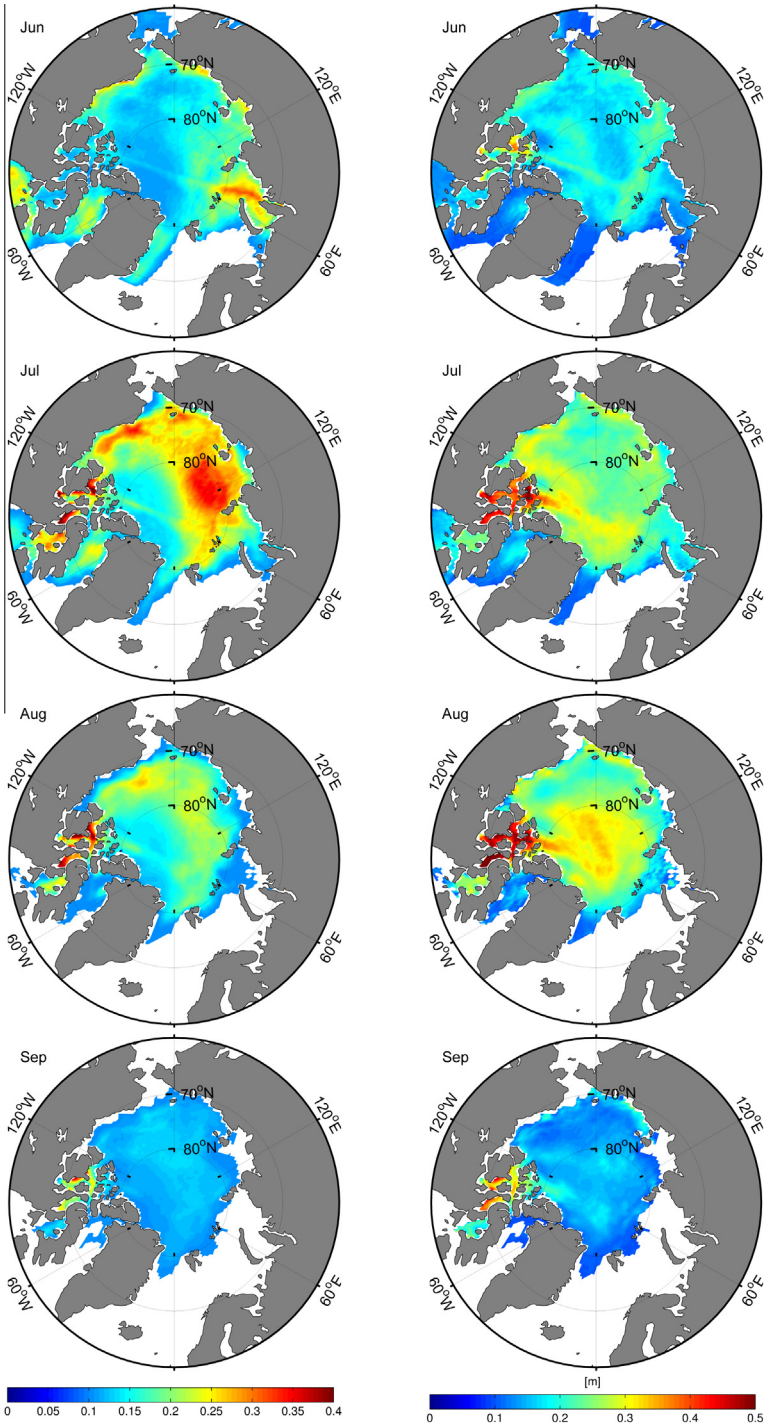

Fig. 8. Average spatial distributions of melt pond fraction of ice (left) and depth (right, in meters) through June-September (downwards) over Arctic sea ice, for the 1982–2011 period.

IceBridge product (Kurtz and Farrell, 2011; Kwok et al., 2011) and in other snow observation works (Gerland et al., 2014).

Although the average annual melt pond fraction cycle over 2000–2011 is in relatively good agreement with MODIS observations (Fig. 7), its seems lower than in existing studies. In Flocco et al. (2012) (same melt pond scheme), their total and exposed melt pond fractions were reaching a maximum of 0.33 and 0.2 in average, respectively, against 0.28 and 0.15 in our control run. In the control simulation of Hunke et al. (2013) (different melt pond scheme), the maximum pond fraction of ice area was ~0.4 and the maximum pond fraction of a grid cell was 0.19 (against ~0.15 in our case). The reason for this underestimation of the mean annual cycle of pond fractions is the lack of melt ponds in the western Arctic Basin, as compared to both MODIS observations (see Figs. 8 and 9) and and those studies (Flocco et al., 2012, especially). Apart from this shortcoming, melt ponds in CTL are are consistent with the latter studies, especially in terms of spatial variability. Both Flocco et al. (2012) and Hunke et al. (2013) had large melt pond fractions

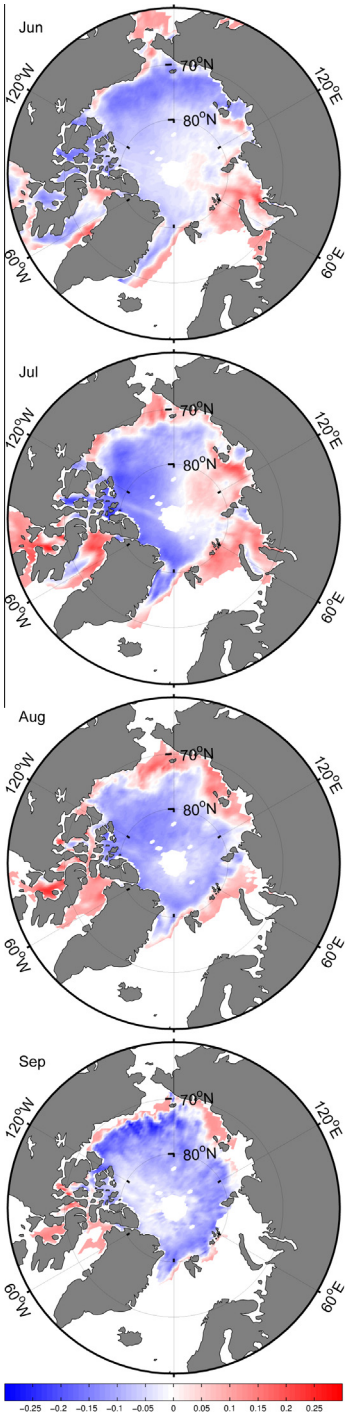

Fig. 9. Average spatial distributions of the difference between modeled and observed pond fractions (of grid cell) over 2000–2011.

in July in the eastern basin (fractions of ~0.3–0.35) and in the Canadian Archipelago, like in CTL. The geographical distribution of melt pond depths in our control run (in July) is also very consistent with those of the two mentioned studies, with the deepest ponds (0.3 to 0.5 m) along the north coasts of Greenland and Canada. The regional variability of melt ponds in the simulation highlights patterns in opposition between pond depth and fractional coverage, particularly in the Central Arctic and the East Siberian Sea. This is characteristic of the melt pond scheme behavior. A shallow but spread out melt pond regime is observed on FYI, while concentrated and deeper melt ponds form atop MYI with a pronounced topography (also confirmed by Fig. 14). In addition, Flocco and Feltham (2007) showed that their model is very sensitive to the snow volume on top of sea ice, that can partially or even totally conceal the ponds. This provides the physical reason for the lack of melt ponds on the MYI of the western and central Arctic Basin in CTL, where some snow persists throughout the summer (Fig. 11).

6. Sensitivity study: impacts of blowing snow on sea ice and melt ponds

6.1. Results

In this section, we take advantage from having melt ponds and blowing snow both represented in our sea ice model to study the impacts of enhanced wind-transport of snow on melt pond distributions. So as to do this, CTL is compared to a second simulation called BSE (blowing snow enhanced simulation), in which the blowing snow tuning parameter γ was increased to 10^{-4} kg m^{-2}. Raising the value of this parameter practically increases the mass flux of snow removed from the pack when winds are strong enough for the snow drift process to occur. As mentioned previously, this parameter is under-constrained owing to lacking observations of wind-blown snow redistribution on sea ice, so the choice of its value for BSE was simply made keeping a compromise between getting noticeable differences in model outputs (BSE vs. CTL) and avoiding unrealistically strong transport rates. In part of the analysis, we distinguish the impacts on MYI from those on FYI.

6.1.1. Impact on sea ice volume

The mean annual cycles of sea ice extent and volume from BSE simulation, are compared to those from CTL in Fig. 10. Only small differences are observed between the two cycles of sea ice extent, with a summer minimum slightly lower in BSE than CTL (6.1 against 6.5×10^6 km^2). By contrast, the sea ice volume in BSE is systematically lower than in CTL throughout the year, with a winter maximum and a summer minimum decreased by 0.7 and 1.0×10^3 km^3, respectively. In summer, the latter difference translates into a volume loss of about 10% with respect to CTL. Fig. 11 shows that this volume loss is exclusively experienced by MYI, with a 10–15 cm lower mean ice thickness in BSE, while the annual cycle of FYI thickness is almost identical in both simulations.

6.1.2. Snow depth changes

As illustrated by Figs. 11 and 12, the primary effect of enhanced wind-transport of snow in the model is to reduce the snow depth

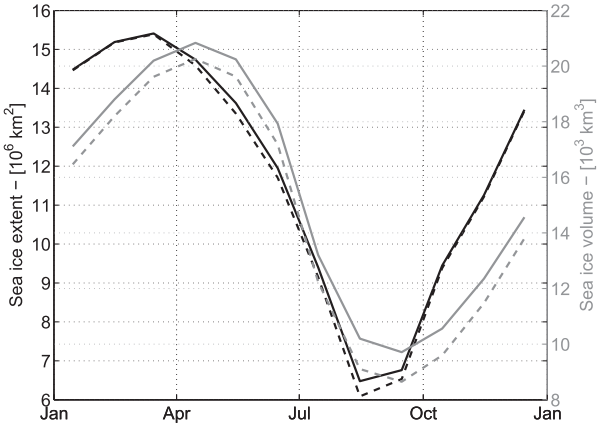

Fig. 10. Mean annual cycles of sea ice extent (in black) and volume (gray) over 1982–2011 for CTL (solid lines) and BSE (dashed lines) simulations.

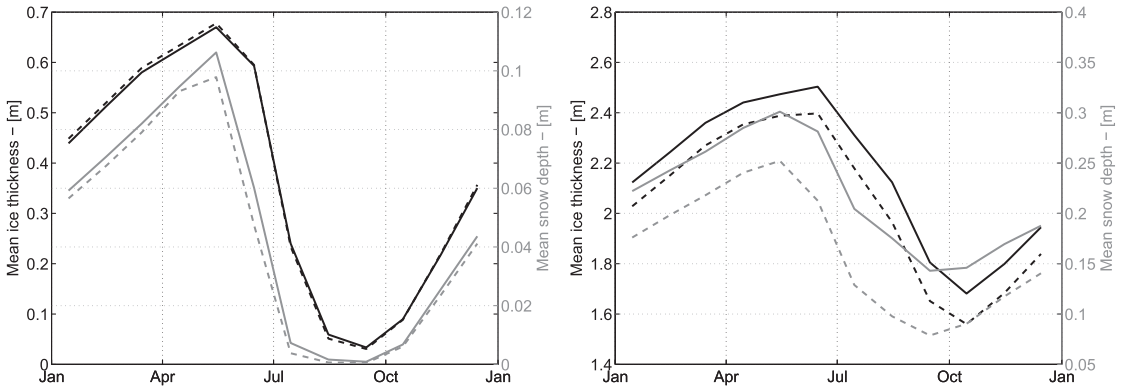

Fig. 11. Mean annual cycles of ice thickness (black) and snow depth (gray) for CTL (solid) and BSE (dashed), computed over FYI (left) and MYI (right), through 1982–2011.

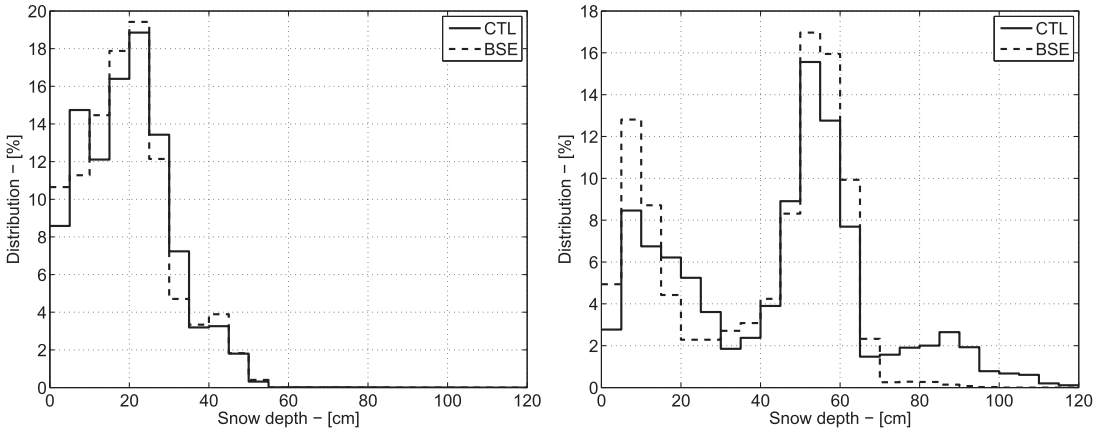

Fig. 12. May snow depth distributions for CTL (solid lines) and BSE (dashed lines), averaged over the FYI (left) and MYI (right) area, over 1982–2011.

on sea ice by removing it from the pack and transferring it into leads during the redistribution process. Therefore, the MYI snow depth distributions of BSE (in May, at the onset of melt pond formation) are clearly shifted towards thinner snow. In BSE, snow deeper than 70 cm, that represents ∼13% of the snow pack in CTL, has virtually disappeared, whereas the proportion of 0–20 cm deep snow has increased by 10%. This snow thinning effect is much less noticeable on FYI. An explicit bimodal SDD is again observable on MYI in both simulations, with peaks at 10 and 55 cm of snow that are all the more distinct in case of stronger erosion (BSE).

6.1.3. Impacts on melt pond distributions

The SDDs at the onset of the melting season impact on the melt pond development in the simulations. Fig. 13 shows that the main effect of the overall reduced snow depths on Arctic sea ice is a small increase in average melt pond fraction (∼3%) and depth (2.5 cm). Nonetheless, those global diagnostics hide interesting changes on MYI, as suggested by Fig. 14, which depicts the changes in melt pond fractional coverage and depth between CTL and BSE for each ice type (i.e., FYI and MYI). The maximum melt pond area and depth on FYI seems to decrease in BSE, as compared to CTL, but those differences are very small (-1% and −0.5 cm, respectively). In contrast, the MYI melt pond cover in BSE exhibits a faster development, which leads to more considerable changes in both fractional coverage (+ 5% coverage) and depth (+ ∼4 cm). The observed magnitude of the changes in melt pond distribution between the two simulations are consistent with those in SDD. Interestingly,

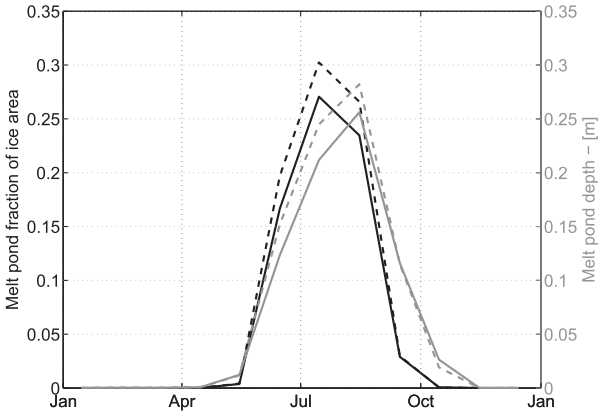

Fig. 13. 1982–2011 mean seasonal cycles of melt pond fraction (black) and depth (gray) for CTL (solid lines) and BSE (dashed lines) simulations.

although the changes on FYI are weak, they suggest a melt pond regime that differs from the one on MYI, with a melt pond volume seemingly decreasing in BSE (further discussed in Section 6.2).

6.2. Discussion

Figs. 13 and 14 suggest that, on average over the whole pond-covered ice and on MYI specifically, increased snow drift leads to

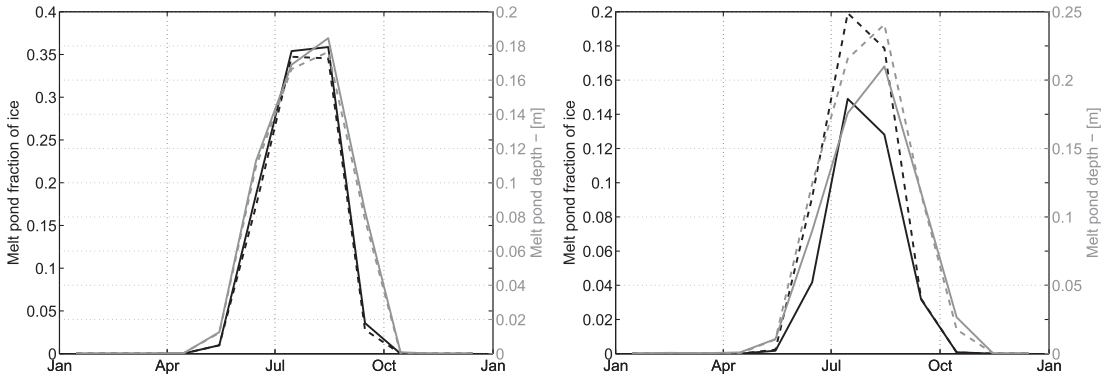

Fig. 14. 1982–2011 mean seasonal cycles of melt pond fraction (black) and depth (gray) for CTL (solid lines) and BSE (dashed lines) simulations, and for each ice type (FYI on the left; MYI on the right).

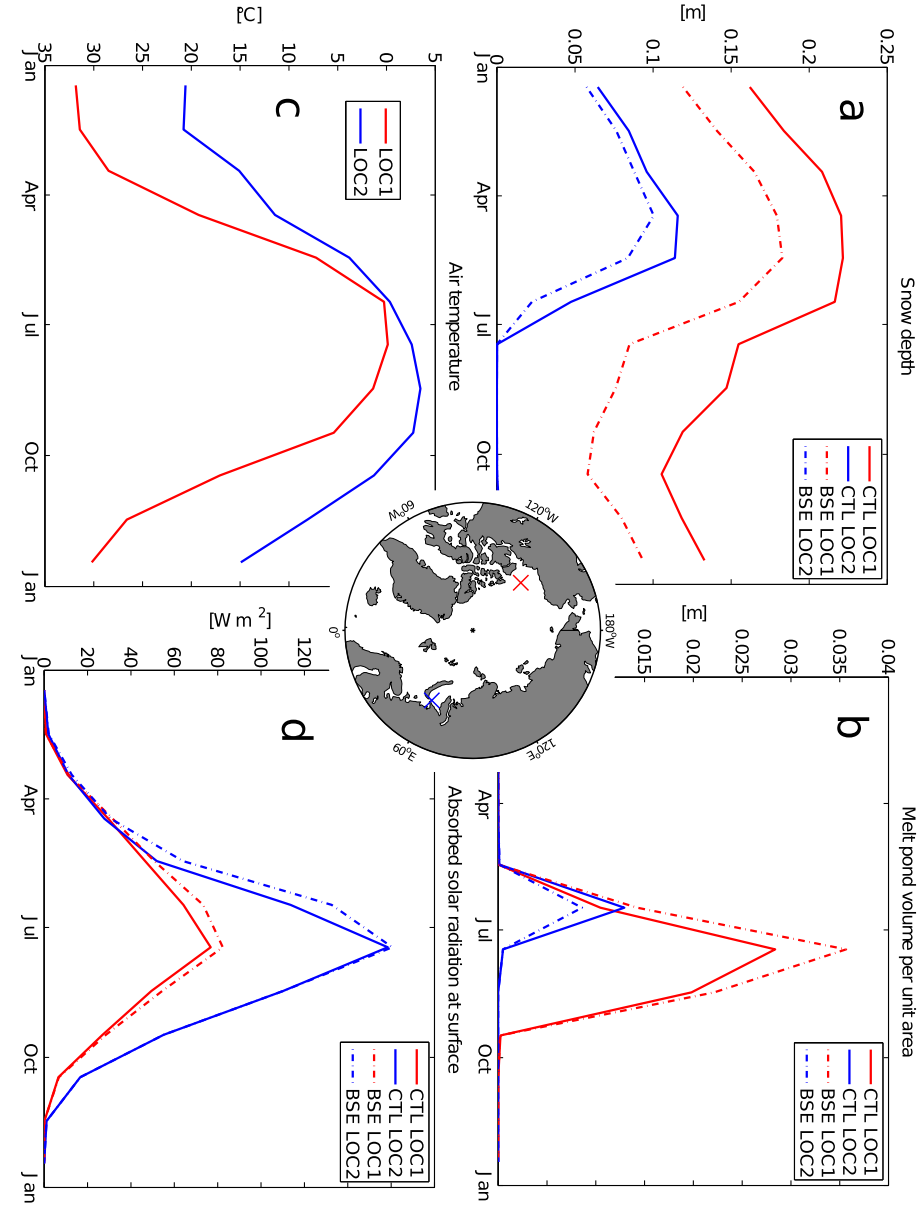

Fig. 15. 1982–2011 climatologies of (a) snow depth, (b) melt pond volume, (c) air temperature and (d) absorbed solar radiation at the snow/ice surface, at two locations of the Arctic Basin. Those locations are shown on the central map. The first (LOC1, in red) is on MYI, and the second (LOC2, in blue) on FYI. Solid and dashed lines depict the climatologies for CTL and BSE simulations, respectively. (For interpretation of the references to colour in this figure caption, the reader is referred to the web version of this article.)

increased pond volume. On the other hand, the FYI melt pond cover seems to respond differently. The first physical reason for these differences in response lies in the primary effect of the blowing snow process in the model: sending a fraction of the sea ice snow cover into leads. The second mechanism, altering the shape of snow depth distributions, is unexpectedly hardly effective in this case. This may be due to inadequate criteria for snow redistribution among ice thickness categories and stresses the need for future improvements of this parameterization. The resulting snow thinning is illustrated in Figs. 11 and 12. In the simulations, snow does not entirely melt away in MYI regions and the blowing snow process influences the snow depth distributions both during winter and after the onset of the melt season. Note that this may not be realistic since snow melts completely in summer at the North Pole buoys sites (Perovich et al., 2014). In case of a greater wind-transport of snow, such as in BSE, less snow is available on sea ice to hide melt ponds and impede their development (as shown in Fig. 14). The overall increased melt pond fraction in this simulation in turn results in increased ice melt through the ice-albedo feedback and explains the lower MYI volume, as compared to CTL (see Figs. 10 and 11, right panel).

The latter mechanism was not necessarily to be expected since, for instance, the opposite consequence was observed in Flocco et al. (2012) in which a simulation with increased precipitation led to more snow available to melt and feed the ponds. Nonetheless, those two behaviors are not inconsistent and are due to the specific influence of our blowing snow parameterization on FYI and MYI. Less (more) snow leading to smaller (larger) melt pond area is to be expected when the total snow cover is melted whatever its depth, which is the case on FYI of both simulations (see Fig. 11). FYI however, once it starts forming, quickly reaches high concentrations and covers most of a model grid cell, meaning that when snow is blown by winds, little is lost into the ocean and most of it is redeposited on the ice it was removed from. Fig. 12 left panel clearly underlines the reduced effect of blowing snow redistribution on FYI. Eventually, when the open water fraction is large enough in summer to capture snow, most of it is already melted and filling in melt ponds. Besides, independently of the snow cover on flat FYI, the liquid meltwater volume transportable on such ice is naturally limited by its topography. As a consequence, FYI in the model might naturally tend to fill with meltwater at full capacity anyway and be less sensitive to the overlying snow volume prior to the onset of the melting season. Thus, strengthened snow drift has little influence on melt pond formation on FYI (Fig. 14), which also explains the rather weak impact at the basin scale (Fig. 13).

Fig. 14 (left panel) does not only suggest a reduced sensitivity of FYI to wind-blown snow redistribution. It also seems to reveal that the impact of enhanced snow drift on FYI melt pond formation tends to be the opposite of its counterpart on MYI ponds. One question then remains unanswered: what are the physical reasons for one model behavior to occur instead of the other? In order to address this issue, we chose two specific locations in the Arctic where the same effect of increased snow drift on snow depth leads to opposite changes in melt pond volume. The climatologies (1982–2011) of snow depth, melt pond volume, air temperature and absorbed solar radiation at the sea ice/snow surface for these two places are displayed in Fig. 15. For both locations, increased wind-transport of snow leads to a snow thinning (panel a). The amplitude of those changes is expectedly different, since those two ice points are part of different ice covers (i.e., MYI and FYI). However, because snow is thinner and air temperature higher at location 2 (panel c), snow melts and disappears much faster in summer than at location 1, also explaining the sharper increase in absorbed solar radiation at the surface (panel d). Since less snow is available to melt in BSE (as compared to CTL), ice surface melt contributes earlier to feeding the ponds. As the ice gets thinner by this process, its capacity to retain surficial meltwater diminishes and the resulting maximum melt pond volume is smaller too (panel b). Naturally, melt ponds at location 2 are ephemeral, and disappear as the ice melts entirely in July.

Hence, two distinct causal connections can be highlighted between snow and melt pond formation, depending on air temperature conditions and snow depth prior to the melt onset. The first, in presence of a resilient snow cover that curtails the surface melting rates and hides the liquid water at the ice surface, relates thicker snow to reduced melt pond development. The second, probably typical of seasonal sea ice carrying a thinner snow cover, is the converse relationship. In the latter configuration, the amount of snow predetermines the timing of the ice thinning and ultimately the one at which ice thickness becomes a limitation factor for water accumulation at its surface.

Finally, it should be noted that the MYI volume being more sensitive than FYI to the effects of wind-blown snow on melt ponds, in spite of the pond area being biased low on MYI, may be counterintuitive. However, since the MYI thickness is also biased low, its sensitivity to changes in the pond coverage may be overestimated (Holland et al., 2006). Besides, the small differences observed between CTL and BSE in Fig. 14 (FYI, left panel) and Fig. 15 for location 2 might be lessened by the averaging effect over years, in relation to year-to-year signals.

7. Conclusion

In order to study the influence of the sea ice late-spring snow cover on the development of melt ponds and the large-scale implications for sea ice, the explicit melt pond model of Flocco and Feltham (2007) was incorporated into a coupled ocean–sea ice model including an advanced snow representation and a blowing snow parameterization. The comparison of a control simulation with MODIS satellite observations over the 2000–2011 period demonstrates a relatively good model ability to reproduce the spatial variability of melt pond depth and a proper mean annual cycle of melt pond fraction on average over the Arctic Basin. However, even keeping in mind the degree of uncertainty of MODIS melt pond fractions, the model seems to fail in simulating satisfactory pond fractions on MYI, where the concealing effect of persistent snow curtails the horizontal development of melt ponds. This results in an underestimation of pond fraction by up to 0.2 in the western basin, along the northern coasts of Greenland and Canada, while flat FYI regions of the peripheral basin are sometimes overcovered by ponds. A difference in maximum of the mean melt pond fraction of about 5 to 10% toward smaller pond area is observed compared to Flocco et al. (2012) and Hunke et al. (2013). As in those studies, the sea ice volume in our control run compared to a no-pond configuration (Lecomte et al., 2013) is much lower (up to 50% volume loss) due to the ice-albedo feedback. Consistently, the simulated late-spring ITD compared to the IceBridge dataset exhibits an excessive proportion of 0.7–2.3 m thick ice, while it lacks ice in the thickest two categories of the model (2.3–5.5 m). The comparison of corresponding SDDs versus IceBridge observations therefore shows a slight bias toward thinner snow as well, which is characterized by an overestimation of very thin snow (0–5 cm). In spite of this, the tail of the SDDs remains in good agreement with observations.

The main effect of the blowing snow parameterization is to reduce snow depth on sea ice by sending a fraction of the transported snow into the leads. Increasing the intensity of snow redistribution by winds therefore subserves further snow thinning in the associated simulation. Quite surprisingly, the snow drift intensity does not change the shape of the simulated snow depth distributions much, which may be due to inadequate erosion or

redistribution criteria in the blowing snow scheme. From there, two melt pond regimes and causal relationships are clearly identified. On MYI, where some snow persists through the summer, the smaller snow volume ensuing from enhanced snow drift has a weaker concealing effect on melt ponds, and facilitates their development. In an other situation, apparently more typical of FYI, a combined effect of higher air temperatures and relatively thin snow makes it a snow cover that entirely melts in summer. Hence, less snow leads to faster sea ice thinning and smaller pond fractions since the amount of freshwater potentially retained at the surface, already limited on FYI, is decreased. The magnitude of such changes is thus smaller than those observed on MYI. The enhanced melt pond formation on MYI in case of increased wind-blown snow redistribution is thus substantially lessened if observed in average over the whole Arctic sea ice cover. Even so, it is influential enough to cause a 10% summer ice volume loss, with regard to our control simulation. It should be stated that our results might be influenced by the number of ice thickness categories in the model given potential sensitivity of both our blowing snow parameterization and the melt pond scheme (Flocco and Feltham, 2007; Flocco et al., 2010) to that parameter. Additionally, the implemented parameterization for wind-blown snow redistribution is very simple and should be improved in future works.

Ultimately, the particular behavior of the blowing snow parameterization and the specific melt pond regimes on FYI as opposed to MYI raises two issues still needing to be addressed. The first concerns the respective sensitivity of FYI and MYI to snow-related processes and properties in sea ice models, in general. Going further, the second regards the actual benefits of including detailed snow parameterizations into sea ice – ocean models running under current climate conditions, i.e., sustaining a progressive transition of sea ice towards a FYI exclusive cover.

Acknowledgements

This work was partly funded by the European Commissions 7th Framework Programme under Grant Agreement number 226520, COMBINE project (Comprehensive Modelling of the Earth System for Better Climate Prediction and Projection). Olivier Lecomte thanks Katherine Leonard, Rob Massom and Ted Maksym for very helpful conversations on the snow redistribution by wind during the SIPEX-II (Sea Ice Physics and Ecosystem eXperiment) field experiment, that took place on East-Antarctic sea ice from September to November 2012. We also thank Bernard Barnier, for the support provided regarding the DFS5 forcing dataset, William Perrie, Editor-in-Chief for Ocean Modelling, Elizabeth Hunke and two other anonymous reviewers for their thorough reviews of our manuscript, which greatly helped improving its quality.

References

Berliand, M., Strokina, T., 1980. Global distribution of the total amount of clouds. Hydrometeorological, Leningrad, 71.
Bitz, C., Lipscomb, W., 1999. An energy-conserving thermodynamic model of sea ice. J. Geophys. Res. 104, 15669–15677.
Bouillon, S., Morales Maqueda, M., Legat, V., Fichefet, T., 2009. An elastic–viscous–plastic sea ice model formulated on Arakawa B and C grids. Ocean Modell. 27, 174–184.
Brodeau, L., Barnier, B., Treguier, A., Penduff, T., Gulev, S., 2010. An ERA40-based atmospheric forcing for global ocean circulation models. Ocean Modell. 31, 88–104.
Cheng, B., Vihma, T., Pirazzini, R., Granskog, M., 2006. Modelling of superimposed ice formation during the spring snowmelt period in the Baltic Sea. Ann. Glaciol. 44, 139–146.
Comiso, J., Nishio, F., 2008. Trends in the sea ice cover using enhanced and compatible AMSR-E, SSM/I, and SMMR data. J. Geophys. Res. 113, C02S07.
Dai, A., Trenberth, K., 2002. Estimates of freshwater discharge from continents: latitudinal and seasonal variations. J. Hydrometeorol. 3, 660–687.
Dee, D., Uppala, S., Simmons, A., Berrisford, P., Poli, P., Kobayashi, S., Andrae, U., Balmaseda, M., Balsamo, G., Bauer, P., et al., 2011. The ERA-Interim reanalysis: configuration and performance of the data assimilation system. Quart. J. Roy. Meteorol. Soc. 137, 553–597.
Déry, S., Tremblay, L., 2004. Modeling the effects of wind redistribution on the snow mass budget of polar sea ice. J. Phys. Oceanography 34, 258–271.
Déry, S., Yau, M., 2002. Large-scale mass balance effects of blowing snow and surface sublimation. J. Geophys. Res. – Atmos 107, ACL-8.
Dussin, R., Barnier, B., 2013. The Making of DFS 5.1. personnal communication, <http://www.drakkar-ocean.eu/forcing-the-ocean>.
Eicken, H., Grenfell, T., Perovich, D., Richter-Menge, J., Frey, K., 2004. Hydraulic controls of summer Arctic pack ice albedo. J. Geophys. Res.–Oceans 109.
Feltham, D., Untersteiner, N., Wettlaufer, J., Worster, M., 2006. Sea ice is a mushy layer. Geophys. Res. Lett., 33.
Fetterer, F., Untersteiner, N., 1998. Observations of melt ponds on Arctic sea ice. J. Geophys. Res. – Oceans 103, 24821–24835.
Fichefet, T., Morales Maqueda, M., 1997. Sensitivity of a global sea ice model to the treatment of ice thermodynamics and dynamics. J. Geophys. Res. – Oceans, 102.
Flocco, D., Feltham, D., 2007. A continuum model of melt pond evolution on Arctic sea ice. J. Geophys. Res. 112, C08016.
Flocco, D., Feltham, D., Turner, A., 2010. Incorporation of a physically based melt pond scheme into the sea ice component of a climate model. J. Geophys. Res. 115, C08012.
Flocco, D., Schroeder, D., Feltham, D., Hunke, E., 2012. Impact of melt ponds on Arctic sea ice simulations from 1990 to 2007. J. Geophys. Res. – Oceans 117.
Freitag, J., Eicken, H., 2003. Meltwater circulation and permeability of Arctic summer sea ice derived from hydrological field experiments. J. Glaciol. 49, 349–358.
Gerland, S., Haas, C., Wang, C., Granskog, M., Haapala, J., Makshtas, A., 2014. Snow thickness distributions over sea ice in the vicinity of the North Pole, 2005–13. In: 2014 IGS International Symposium on Sea Ice in a Changing Environment, Hobart, Tas., 10–14 Mar. 69A668.
Girard, L., Bouillon, S., Weiss, J., Amitrano, D., Fichefet, T., Legat, V., 2011. A new modeling framework for sea-ice mechanics based on elasto-brittle rheology. Ann. Glaciol. 52, 123–132.
Golden, K., Eicken, H., Heaton, A., Miner, J., Pringle, D., Zhu, J., 2007. Thermal evolution of permeability and microstructure in sea ice. Geophys. Res. Lett., 34.
Goosse, H., 1997. Modeling the large-scale behavior of the coupled ocean-sea ice system (Ph.D. thesis). Université Catholique de Louvain, Louvain-la-Neuve, Belgium.
Goosse, H., Fichefet, T., 1999. Importance of ice–ocean interactions for the global ocean circulation: a model study. J. Geophys. Res. 104, 23337–23355.
Holland, M., Bitz, C., Hunke, E., Lipscomb, W., Schramm, J., 2006. Influence of the sea ice thickness distribution on polar climate in CCSM3. J. Climate 19, 2398–2414.
Holland, M., Bailey, D., Briegleb, B., Light, B., Hunke, E., 2012. Improved sea ice shortwave radiation physics in CCSM4: the impact of melt ponds and aerosols on Arctic sea ice. J. Climate 25, 1413–1430.
Hunke, E., Dukowicz, J., 1997. An elastic–viscous–plastic model for sea ice dynamics. J. Phys. Oceanography 27, 1849–1867.
Hunke, E., Hebert, D., Lecomte, O., 2013. Level-ice melt ponds in the Los Alamos sea ice model, CICE. Ocean Modell. 71, 26–42.
Järvinen, O., Lepparanta, M., 2011. Transmission of solar radiation through the snow cover on floating ice. J. Glaciol. 57, 861–870.
Jordan, R., Albert, M., Brun, E., 2008. Physical processes within the snow cover and their parameterization. In: Armstrong, R., Brun, E. (Eds.), Snow and Climate: Physical Processes, Surface Energy Exchange and Modeling. Cambridge University Press, pp. 12–69.
Kalnay, E., Kanamitsu, M., Kistler, R., Collins, W., Deaven, D., Gandin, L., Iredell, M., Sana, S., White, G., Woollen, J., et al., 1996. The NCEP/NCAR 40-year reanalysis project. Bull.-Am. Meteorol. Soc. 77, 437–471.
King, J., Pomeroy, J., Gray, D., Fierz, C., Föhn, P., Harding, R., Jordan, R., Martin, E., Plüss, C., 2008. Snow-atmosphere energy and mass balance. In: Armstrong, R., Brun, E. (Eds.), Snow and Climate: Physical Processes, Surface Energy Exchange and Modeling. Cambridge University Press, pp. 70–124.
Kurtz, N., Farrell, S., 2011. Large-scale surveys of snow depth on Arctic sea ice from operation icebridge. Geophys. Res. Lett. 38, L20505.
Kurtz, N., Studinger, M.S., Harbeck, J., Onana, V., Farrell, S., 2012, updated 2013. IceBridge sea ice freeboard, snow depth, and thickness. NASA DAAC at the National Snow and Ice Data Center, Boulder, Colorado, USA. <http://nsidc.org/data/idcsi2.html>.
Kwok, R., Panzer, B., Leuschen, C., Pang, S., Markus, T., Holt, B., Gogineni, S., 2011. Airborne surveys of snow depth over Arctic sea ice. J. Geophys. Res. 116, C11018.
Large, W., Yeager, S., 2004. Diurnal to decadal global forcing for ocean and sea-ice models: the data sets and flux climatologies. NCAR Tech. Note TN-460+ STR.
Lecomte, O., Fichefet, T., Vancoppenolle, M., Nicolaus, M., 2011. A new snow thermodynamic scheme for large-scale sea-ice models. Ann. Glaciol. 52, 337–346.
Lecomte, O., Fichefet, T., Vancoppenolle, M., Domine, F., Massonnet, F., Mathiot, P., Morin, S., Barriat, P., 2013. On the formulation of snow thermal conductivity in large-scale sea ice models. J. Adv. Model. Earth Syst. 5, 542–557.
Leonard, K., Maksym, T., 2011. The importance of wind-blown snow redistribution to snow accumulation on Bellingshausen Sea ice. Ann. Glaciol. 52, 271–278.
Levitus, S., 1998. NODC World Ocean Atlas, <http://www.esrl.noaa.gov/psd/>.
Madec, G., 2008. NEMO ocean engine: note du Pole de Modelisation, Institut Pierre-Simon Laplace.
ICDC Modis, 2013. Arctic melt pond cover fractions were obtained for 2000–2011 from the Integrated Climate Data Center (ICDC, <http://icdc.zmaw.de/>), University of Hamburg, Hamburg, Germany.
Pedersen, C., Roeckner, E., Lüthje, M., Winther, J., 2009. A new sea ice albedo scheme including melt ponds for ECHAM5 general circulation model. J. Geophys. Res. – Atmos. 114.

Perovich, D., Grenfell, T., Light, B., Hobbs, P., 2002. Seasonal evolution of the albedo of multiyear Arctic sea ice. J. Geophys. Res. – Oceans 107, SHE-20.
Perovich, D., Richter-Menge, J., Polashenski, C., Elder, B., Arbetter, T., Brennick, O., 2014. Sea ice mass balance observations from the North Pole Environmental Observatory. Geophys. Res. Lett. 41, 2019–2025.
Petrich, C., Eicken, H., Polashenski, C., Sturm, M., Harbeck, J., Perovich, D., Finnegan, D., 2012. Snow dunes: a controlling factor of melt pond distribution on Arctic sea ice. J. Geophys. Res. – Oceans, 117.
Polashenski, C., Perovich, D., Courville, Z., 2012. The mechanisms of sea ice melt pond formation and evolution. J. Geophys. Res. – Oceans, 117.
Rösel, A., Kaleschke, L., Birnbaum, G., 2012. Melt ponds on Arctic sea ice determined from MODIS satellite data using an artificial neural network. The Cryosphere 6, 431–446.
Schmidt, R., 1982. Properties of blowing snow. Rev. Geophys. 20, 39–44.
Scott, F., Feltham, D., 2010. A model of the three-dimensional evolution of Arctic melt ponds on first-year and multiyear sea ice. J. Geophys. Res. – Oceans 115.
Shine, K., Henderson-Sellers, A., 1985. The sensitivity of a thermodynamic sea ice model to changes in surface albedo parameterization. J. Geophys. Res. – Atmos. 90, 2243–2250.
Simmons, A., Uppala, S., Dee, D., Kobayashi, S., 2007. ERA-interim: new ECMWF reanalysis products from 1989 onwards. ECMWF Newslett. 110, 25–35.
Sturm, M., Massom, R., 2009. Snow and sea ice. In: Thomas, D.N., Dieckmann, G. (Eds.), Sea Ice. Wiley-Blackwell, pp. 153–204 (second ed., chapter 5).
Sturm, M., Holmgren, J., Perovich, D., 2002. Winter snow cover on the sea ice of the Arctic Ocean at the Surface Heat Budget of the Arctic Ocean (SHEBA): temporal evolution and spatial variability. J. Geophys. Res. 107.
Sugiura, K., Nishimura, K., Maeno, N., Kimura, T., 1998. Measurements of snow mass flux and transport rate at different particle diameters in drifting snow. Cold Regions Sci. Technol. 27, 83–89.
Trenberth, K., Large, W., 1989. European Center for Medium Range Weather Forecasts. A global ocean wind stress climatology based on the ECMWF analyses.
Vancoppenolle, M., Fichefet, T., Goosse, H., Bouillon, S., Madec, G., Maqueda, M., 2009. Simulating the mass balance and salinity of Arctic and Antarctic sea ice. 1. Model description and validation. Ocean Modell. 27, 33–53.
Webster, M., Rigor, I., Nghiem, S., Kurtz, N., Farrell, S., Perovich, D., Sturm, M., 2014. Interdecadal changes in snow depth on Arctic sea ice. J. Geophys. Res. – Oceans.
Zhang, J., Rothrock, D., 2003. Modeling global sea ice with a thickness and enthalpy distribution model in generalized curvilinear coordinates. Month. Weather Rev. 131, 845–861.